CFD modelling of heat transfer and airflow in an insulated box equipped with Phase Change Material Tanathep LEUNGTONGKUM* (a,b) , Onrawee LAGUERRE (a) , Nattawut CHAOMUANG (c) , Alain DENIS (a) and Denis FLICK (b)

Tanathep Leungtongkum, Onrawee Laguerre, Nattawut Chaomuang, Alain Denis, D. Flick

DOI: 10.18462/iir.icr.2023.0556

CFD modelling of heat transfer and airflow in an insulated box equipped with Phase Change Material

Tanathep LEUNGTONGKUM*[(a,b)], Onrawee LAGUERRE[(a)], Nattawut CHAOMUANG[(c)], Alain DENIS[(a)] and Denis FLICK[(b)]

[(a)] Université Paris-Saclay, INRAE, FRISE, 92761 Antony, France
[(b)] Université Paris-Saclay, INRAE, AgroParisTech, UMR SayFood, 91120 Palaiseau, France
[(c)] Department of Food Engineering, School of Engineering, King Mongkut's Institute of Technology Ladkrabang, Bangkok, Thailand 10520
*Corresponding author: Tanathep.leungtongkum@inrae.fr

ABSTRACT

Insulated boxes equipped with Phase Change Material (PCM) are primarily used for the last mile food delivery, as they are simple to use and low-cost. However, these boxes maintain high average temperature and significant temperature heterogeneity in transport. This work presents a numerical study to predict the heat transfer and airflow inside an insulated box (overall heat transfer coefficient 0.9 $W \cdot m^{-2} \cdot K^{-1}$) equipped with PCM (ice, melting point 0°C). Three configurations were studied: an empty box, a box loaded with Extruded Polystyrene (XPS slabs), and a box loaded with test product (Tylose slabs). Computational Fluid Dynamic simulations were performed by ANSYS FLUENT. The numerical results of temperature and velocity fields were compared with experimental values measured by thermocouples and Particle Image Velocimetry, respectively. Good agreement was obtained between the numerical and experimental results, with the maximum difference of 1.5°C and 0.03 $m \cdot s^{-1}$.

Keywords: Insulated boxes, PCM, Airflow, Heat transfer, CFD

1. INTRODUCTION

Insulated boxes equipped with Phase Change Material (PCM) have been widely used in the last-mile delivery of temperature-sensitive products, mainly when refrigeration equipment is unavailable (East et al., 2009). However, spatial and temporal temperature variation during a supply chain currently limit their use (Du et al., 2020; Laguerre et al., 2013). Accurate physical-based models can predict the temperature in a box in which conduction (in walls, unmelted PCM, and products), natural convection (between air and walls/product surface), and radiation occur (Rincón-Casado et al., 2017; Shinoda et al., 2019). These three heat transfer modes are of the same order of magnitude; although several studies reviewed in Leungtongkum et al. (2022) often considered only heat conduction, all three need to be considered (Laguerre & Flick, 2010).

This paper develops a Computational Fluid Dynamic (CFD) model that applies airflow and all heat transfer modes for an insulated box equipped with PCM. The simulation allows the prediction of the temperature field and its evolution with time inside the box for two PCM positions (top and sidewall) and three loading conditions: no load, loaded with insulating material (extruded polystyrene slabs), and with test product (Tylose slabs). The second condition highlights the effect of the inert load as an obstacle on airflow (without heat exchange), while the third represents the realistic food transport conditions. The numerical results of different studied conditions are compared with the experimental ones for validation.

The model developed in this paper can be used to predict the effect of box characteristics such as insulation type, wall thickness, box geometry, and operating conditions such as ambient temperature, load type, and product initial temperature. By combining this model with quality and safety models, product evolution along the supply chain can be assessed.

2. EXPERIMENTAL STUDY

2.1. Materials

Measurement of temperature and air velocity required two different boxes (Fig. 1). Box A was used for the thermal study; it was a commercialized multilayer insulated box (Manutan SA, Gonesse, France) with 500 mm x 310 mm x 300 mm internal dimensions and 570 mm x 380 mm x 370 mm external dimensions. Its walls were made of expanded polystyrene (25 mm thickness), polypropylene (inner and outer layers of 3.5 mm thickness with ε = 0.97 (Vavilov & Burleigh, 2020)), and an air gap between the expanded polystyrene and the inner layer (estimated thickness 5 mm). Box B was used for the airflow study; it had the exact dimensions and wall structure except two side walls made of triple-glazed windows (3 glass panes of 4 mm thickness each, wall emissivity ε = 0.03 (manufacturer data), two argon-filled 10-mm gaps). The overall heat transfer coefficient of these two walls (insulated wall and triple-glazed window) is about 0.90 $W \cdot m^{-2} \cdot K^{-1}$. This value was obtained by calculation based on the thickness and thermal conductivity of the materials used for building the walls, which are listed in Table 1.

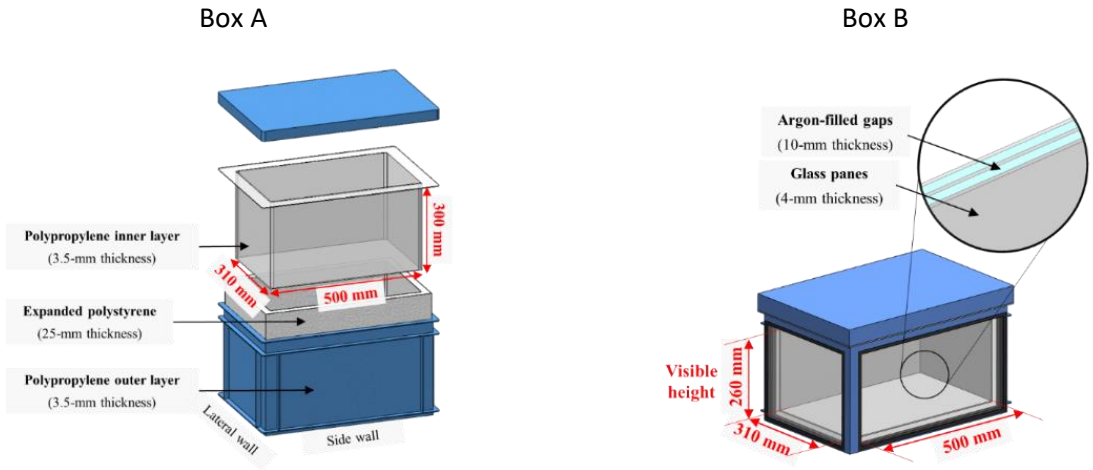

Fig. 1: Boxes used in the study. Box A: a commercial box for temperature measurement and Box B: a box with walls modification by triple-pane windows for velocity measurement.

Table 1: Thermo-physical properties of materials

Material	Density ($kg \cdot m^{-3}$)	C_p ($J \cdot kg^{-1} \cdot K^{-1}$)	k ($W \cdot m^{-1} \cdot K^{-1}$)	Reference
Extruded polystyrene	35	1210	0.029	Cengel and Ghajar (2020)
Polypropylene	910	1925	0.120	Cengel and Ghajar (2020)
Tylose	1070	3372	0.510	Icier and Ilicali (2005)
Water (solid)	920	2040	1.880	Cengel and Ghajar (2020)
Air (5°C)	1.269	1006	0.024	Cengel and Ghajar (2020)
Glass	2225	835	1.4	Cengel and Ghajar (2020)
Argon	-	-	0.018	Roder et al. (2000)

2.2. Thermal study

2.2.1. PCM and test product preparation before experiment

Tap water is used as the PCM for this study (melting temperature close to 0°C). It was first filled into a slab of dimensions 500 mm x 310 mm x 50 mm. The PCM slab was then placed horizontally in a freezer set at -2°C for 48 h to ensure homogenous PCM thickness and temperature. Sixteen packs of the test product (dimensions of a pack 200 mm × 100 mm × 50 mm) were placed in a polystyrene box and stored in a domestic refrigerator set at 4°C 24 hours before each experiment to ensure homogeneous initial product temperature.

2.2.2. Instrumentation

The temperature was measured by T-type thermocouples linked to a data acquisition unit (Agilent 34972A, CA, USA). These thermocouples were previously calibrated at -10°C, 0°C, 10°C, 20°C and 30°C with a precision of ±0.2°C.

2.2.3. Temperature measurement in an unloaded box

Fig. 2a presents an empty box with PCM on a sidewall. The air temperature was measured on the middle plane (x = 250 mm) at different y and z positions using two stands, and each one was equipped with 12 thermocouples spread over the height (z-axis). Three thermocouples were placed inside the PCM (at mid-thickness) and on the surface of the PCM container.

The installed thermocouples were then placed in the box. 90 minutes after the box was closed (when a steady state was reached), temperatures were recorded every 15 seconds for 5 minutes. After these 5 minutes, the box was opened, and the stands were displaced rapidly (to avoid disturbances by external air) before closing the box again. 15 minutes later (when a steady state was reached again), temperatures were recorded every 15 seconds for 5 minutes. Measurements were repeated by changing the positions of the stands, allowing 200 measurement points in total. A temperature contour map was plotted by MATLAB with interpolation from these measurements following the experiment.

2.2.4. Temperature measurement in a loaded box

The loaded box was prepared using the same methodology for two different types of materials. The first material was four XPS slabs (extruded polystyrene 200 mm × 400 mm × 50 mm), and the second was sixteen test product packs previously stored in a domestic refrigerator for 24 hours. Each material was placed in the center of the box. After closing the box, temperatures in the middle plane (x = 250 mm) were measured at 33 positions (Fig. 2b) every 30 seconds for 4 hours without opening the box.

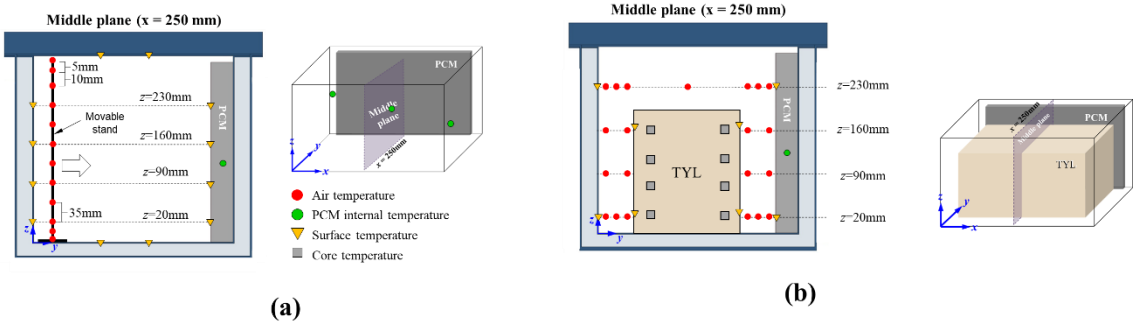

Fig. 2 Diagram showing the experimental setup for temperature measurement for PCM located on the side wall of (a) empty box, and (b) loaded box. TYL = Tylose packages.

2.3. Airflow study

Fig. 3 shows the experimental setup for the air velocity measurement using Particle Image Velocimetry (PIV). A smoke machine (Antari, F-80Z) generated an oil-based smoke tracer (mean diameter 0.3 µm); the smoke

tracer was precooled in a container with four PCM packs to decrease its temperature from 50°C to 10°C. The smoke was then diffused into Box B through a connecting duct using a small fan.

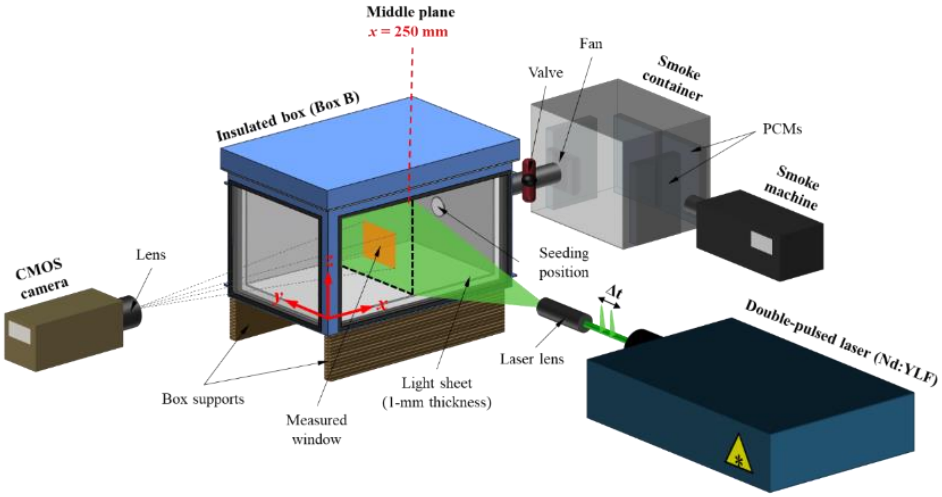

Fig. 3 Diagram showing the PIV setup.

The 2D-PIV system (LaVision, FlowMaster 2D) included three main components (Fig. 3): a double-pulsed Nd:YLF laser (527 nm wavelength, 10 mJ pulse energy), a high-speed 12-bit CMOS video camera (Photron, FASTCAM SA3; 1024 × 1024 pixels in resolution) fitted with a lens (Sigma; 105 mm, f/1:2.8). A programmable timing unit (PTU-X) allowed the synchronization between the laser pulse and the camera. Visualization of the airflow pattern was possible by the smoke particle scattering during laser pulses. Image acquisition and post-processing to obtain the air velocity field were achieved using DaVis 10.0.5 software. The camera and the laser were mounted on a three-dimensional displacement system (precision of displacement ±1 mm); both items were aligned to allow the perpendicularity between the camera view and the light sheet (1-mm thickness).

PIV measurements were performed on the middle plane (x = 250 mm). 500 pairs of images were recorded for each measured window every 20 ms, with a time interval of 900 µs between two images of the same pair (between two laser pulses). More details on image acquisition and post-processing can be found in Leungtongkum et al. (2023).

The measurement was conducted for the box with two PCM positions (top and sidewall) and under three loading conditions: no load, loaded with inert material (extruded polystyrene slabs, XPS), and with test product (Tylose slabs). The second condition demonstrates the effect of the load as an airflow obstacle only (i.e., without heat exchange with air), whereas the third condition demonstrates the effect of the load in a realistic food transport scenario (i.e., where there is heat exchange with air).

3. NUMERICAL STUDY

3.1. Model assumptions

Airflow is laminar, as its Rayleigh number is lower than 10^9 (calculation not shown). The Boussinesq approximation is used (density is assumed constant except in the gravity term). Viscous dissipation into heat is neglected.

The PCM is assumed to be in a melting phase during the whole simulation, so the temperature of its external face is considered constant at 0°C. The convection in melted ice is neglected.

3.2. Governing equations

For air, laminar flow caused by natural convection is considered:

Continuity: $\nabla \cdot (\rho \vec{v}) = 0$ Eq. (1)

Momentum: $\frac{\partial}{\partial t}(\rho \vec{v}) + \nabla \cdot (\rho \vec{v} \vec{v}) = -\nabla P + \nabla \cdot (\mu \nabla \vec{v}) + \rho_{ref} \beta (T - T_{ref}) \vec{g}$ Eq. (2)

Energy: $\frac{\partial}{\partial t}(\rho c_p T) + \nabla \cdot (\rho \vec{v} c_p T) = \nabla \cdot (\lambda \nabla T)$ Eq. (3)

For the load (test product or XPS), only conduction is considered:

Energy: $\frac{\partial}{\partial t}(\rho_p c_{p.p} T) + \nabla \cdot (\rho_p c_{p.p} T) = \nabla \cdot (\lambda_p \nabla T)$ Eq. (4)

where ρ is the density [kg·m^{-3}], $\vec{v}$ is the fluid velocity [m·s^{-1}], P is the pressure [N·m^{-2}], μ is the dynamic viscosity [kg·s^{-1}·m^{-1}], ρ_{ref} is the density at reference temperature [kg·m^{-3}], β is the thermal expansion coefficient [K^{-1}], T is the temperature [°C or K], T_{ref} is the reference temperature = 5°C, $\vec{g}$ is the gravitational acceleration = 9.81 m·s^{-2}, c_p is the specific heat capacity [J·kg^{-1}·K^{-1}] and λ is the thermal conductivity [W·m^{-1}·K^{-1}].

The parameters with index p are for the product (without index is for air).

3.3. Boundary conditions

At PCM wall in contact with internal box walls, constant temperature at 0°C was applied:

T = 0°C Eq. (5)

At PCM wall in contact with internal air, the coupled thermal boundary condition was used with 2.5 mm wall thickness with no slip boundary condition.

At the internal box walls, the following momentum and thermal conditions were applied:

No slip boundary condition: $\vec{v} = 0$ Eq. (6)

Cauchy type thermal boundary condition: $U(T_{amb} - T) = \lambda \nabla T \cdot \vec{n} + q_{rad}$ Eq. (7)

where U is the overall heat transfer coefficient, T_{amb} = 20°C

and $q_{rad} = \varepsilon \sigma T^4 + (1 - \varepsilon) q_{in}$ Eq. (8)

with ε is the wall emissivity

Surface-to-surface radiation was activated, and the radiative flux entering the surface j coming from all the other surfaces i was calculated from

$q_{in,j} = \sum_i F_{ij} q_{rad,i}$ Eq. (9)

where F_{ij} is the view factor of the surface i relating to the surface j

The external area of the box is higher than the internal one; thus, for a global heat balance, the geometric mean of an external and internal area must be used. Since the boundary condition applies on the internal wall, in governing equations for the CFD approach, U is corrected by a factor of $\sqrt{A_{ext}/A_{int}}$.

3.4. Numerical simulation

The geometry was drawn by using SpaceClaim and meshed with ANSYS FLUENT meshing. A mesh independence study was first conducted, which led to considering around 2 x 10^5 cells. The study domain contained between 191850 and 256211 polyhedral cells depending on PCM position and loading conditions.

The numerical study was performed with ANSYS FLUENT 2021 R1 in a transient state. According to a time step independence study, the time step of 1 s was used. For an empty box and a box loaded with XPS, the simulation was performed for 10 min. For a box loaded with Tylose, the simulation was performed for 4 h.

4. RESULTS AND DISCUSSIONS

To highlight the natural convection, first, the experimental and numerical velocity and temperature fields are presented for unloaded boxes with PCM (cold wall) on the side and at the top (Fig. 4 to 7). Then, these fields are presented in the presence of a load in a box with PCM on a sidewall (Fig. 8 to 12) and with PCM at the top (Fig. 13 to 15).

4.1. Air velocity and temperature profiles in an unloaded box with PCM on a sidewall

Fig. 4a and 4b present the observed airflow patterns and temperature fields on the middle plane of the box (x = 250 mm) with PCM on a sidewall. Downward airflow close to the PCM occurs because the air temperature decreases and the air density increases when the air exchanges heat with PCM (Fig. 4a). Upward airflow close to the opposite vertical wall is caused by heat exchange with the vertical warm wall; here, air temperature increases while air density decreases. Air flows from the right to the left near the bottom of the box. PIV measurement was impossible at the top of the box because the laser sheet could not be projected into this zone. However, the law of mass conservation proves that air flows from the left to the right, leading to an airflow recirculation loop. The maximum measured air velocity was around 0.10 $m \cdot s^{-1}$. The corresponding temperature field (Fig. 4b) agrees with the airflow pattern, i.e., the coldest air (0.5°C) was observed at the bottom-right corner after air was cooled down by exchange with PCM. The warmest air (10°C) was observed at the top after it was warmed up by exchange with the box walls.

Simulation results at 10 minutes gave similar air velocity flow patterns (Fig. 4a') and temperature fields (Fig. 4b'). In this simulation, the velocity and temperature fields did not vary from 7 minutes to 10 minutes, implying that a steady state was reached. Fig. 5a compares the experimental and numerical air velocity values in the z-direction and temperature at z = 160 mm. A good agreement between predicted and measured values was observed with a maximum difference in air velocity and temperature of 0.02 $m \cdot s^{-1}$ and 1.2°C, respectively.

(a)

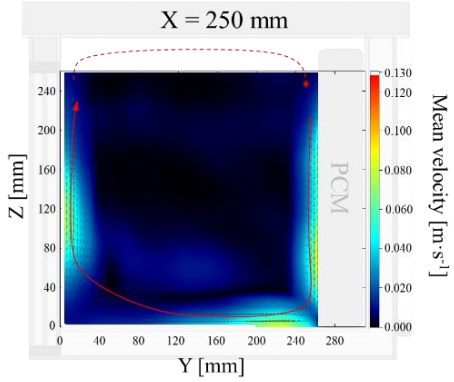

(a')

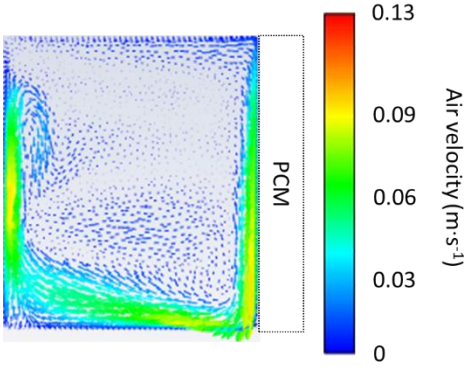

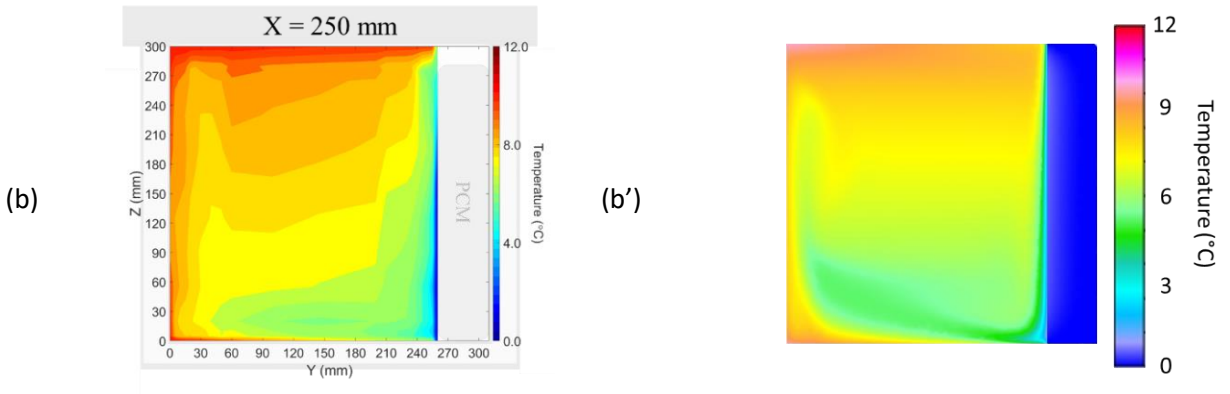

Fig. 4: (a) Experimental air velocity field and (b) experimental temperature field on the middle plane of an unloaded box with PCM on a sidewall. (a') Corresponding numerical air velocity field and (b') Corresponding numerical temperature field.

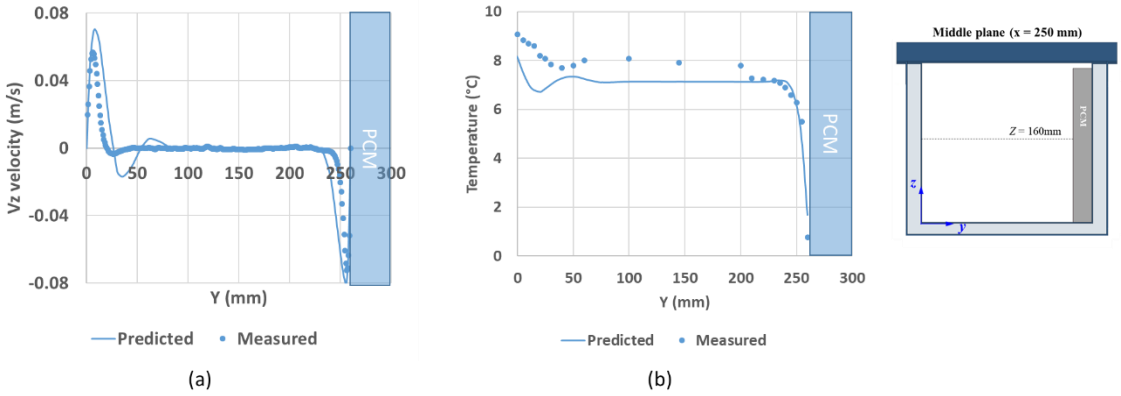

Fig. 5: Comparison between experimental and numerical results at the middle plane and z = 160 mm in an unloaded box with PCM on a sidewall (a) air velocity in the z-direction and (b) air temperature

4.2. Air velocity and temperature profiles in an unloaded box with PCM at the top

Fig. 6 shows the observed airflow patterns (Fig. 6a) and temperature fields (Fig. 6b) on the middle plane of the box (x = 250 mm) with PCM at the top. Two airflow loops are observed, with a downward flow in the middle of the box and an upward flow close to each side wall. Air becomes colder and flows downwards when it exchanges heat with the PCM at the top. The air moves toward the warmer side walls, as its density decreased after reaching the bottom of the box, and it flows upwards until approaching the PCM at the top again. The maximum measured air velocity was about 0.08 $m \cdot s^{-1}$. The visual observation of smoke flow with time showed that the downward flow in the central region was oscillating (result not shown). The corresponding experimental temperature field (Fig. 6b) confirms this flow explanation with the coldest air (4.1°C) at the center of the box just below the PCM surface and the warmest air (8.1°C) near the mid-height of the side walls after the air was warmed up by exchange with the box walls. It is to be highlighted that the velocity shown in Fig. 6a was averaged over 10 seconds, and the temperature in Fig. 6b was averaged over 5 minutes.

The simulation confirms the instability of air velocity: the velocity field varied with time (Fig. 6a') even when the boundary conditions were steady, and the flow was laminar due to the nonlinearity of the Navier-Stokes equations. The temperature field was also unstable (Fig. 6b'). The simulations at 5, 7, and 10 minutes did not give the same air velocity field and temperature distribution; however, it seems that the result at 5 minutes provided good agreement with the measured air velocity field and temperature distribution. Fig. 7 shows a comparison between the experimental and numerical values (at 5, 7, 10 minutes and average between 5 minutes and 10 minutes) of air velocity in the z-direction and temperature at z = 125 mm. On average, the

simulation can capture the trends and the order of magnitude but comparing instantaneous predicted data with time-averaged measured data is difficult.

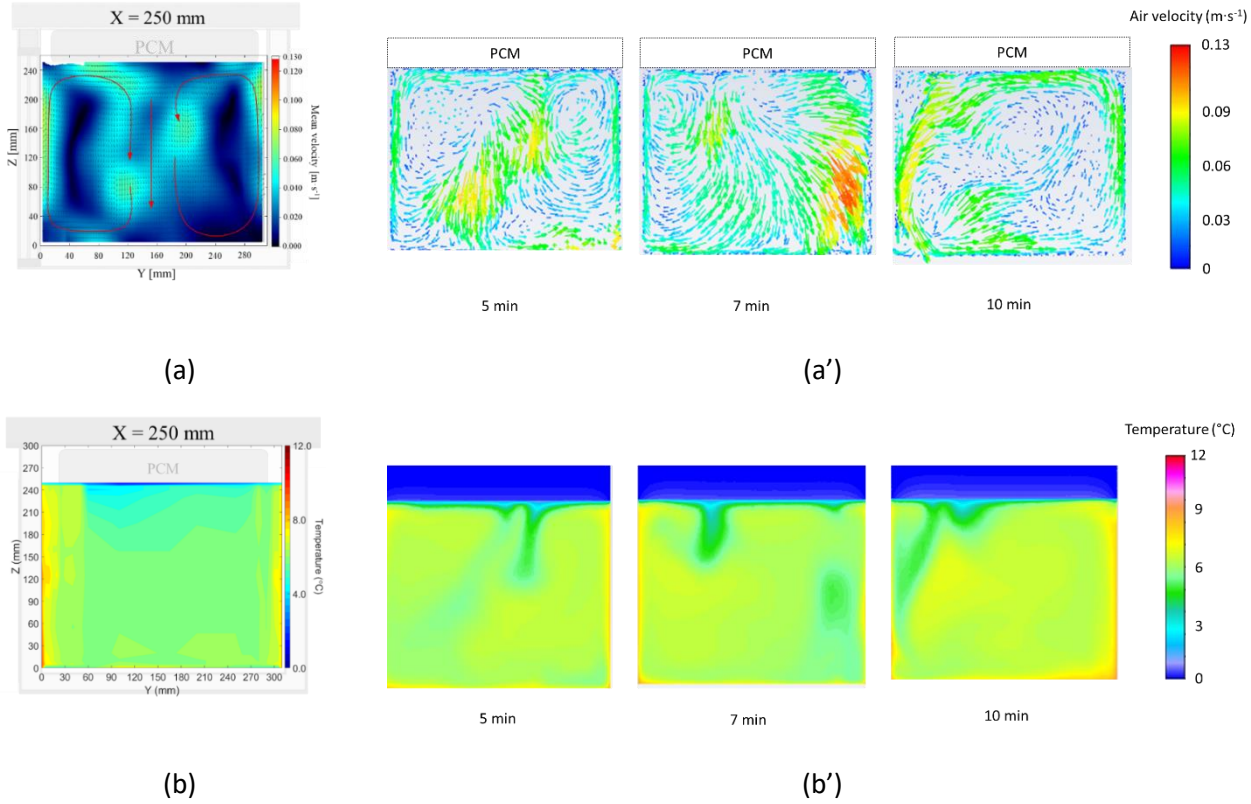

Figure 6: (a) Experimental air velocity field and (b) experimental temperature field on the middle plane of an unloaded box with PCM at the top. (a') and (b') are corresponding numerical results at 5 min., 7 min. and 10 min.

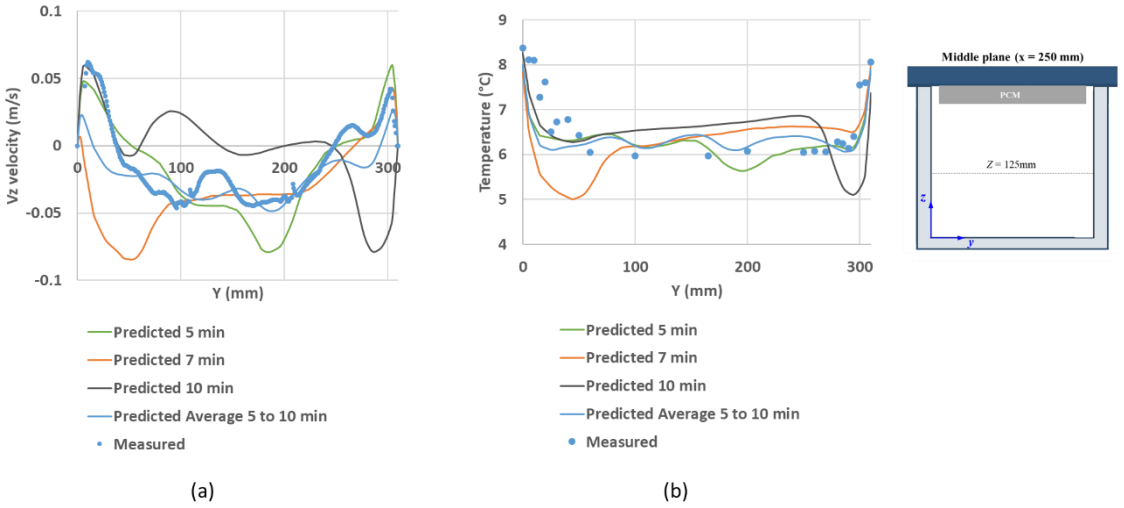

Figure 7: Comparison between experimental and numerical results at t = 5 min., 7 min., 10 min. and average between 5 min. and 10 min. in an unloaded box with PCM at the top at the middle plane and z = 125 mm of (a) air velocity in the z-direction and (b) air temperature

4.3. Air velocity and temperature profiles in a loaded box with PCM on a sidewall

Fig. 8a and 9a present the observed airflow patterns on the box's middle plane (X = 250 mm) with PCM on a sidewall and loaded with XPS and Tylose, respectively. In both cases, air flew upwards in the left gap and flew downward in the right gap. The impossibility of laser sheet access into this gap explains the lack of PIV measurements at this position. The maximum measured air velocity was around 0.10 $m \cdot s^{-1}$. Fig. 8b and 9b present the experimental temperature field for the box loaded with XPS and Tylose slabs, respectively. In

both cases, the temperature results agreed with the air velocity field, i.e., increasing temperature along the air-circulation loop after air was cooled down by exchange with PCM.

The numerical simulation gave similar air velocity fields (Fig. 8a' and 9a'), but the predicted temperatures (Fig. 8b' and 9b') were slightly lower than the measured values. The airflow was then analyzed in 3D since air flew around the load, as illustrated in Fig. 10. Air flew downwards and toward the lateral walls in the gap between PCM and load (Fig. 10a) and from the left (near PCM) to the right in the lateral walls (Fig. 10b). Fig. 10c shows the complete air circulation loop.

Fig. 11 compares experimental and numerical air velocity values in the z-direction and temperature at z = 230 mm in a box loaded with Tylose (initial temperature 4.4°C). A good agreement between predicted and measured values can be observed with a maximum air velocity difference of 0.03 $m \cdot s^{-1}$ and a maximum temperature difference of 1.5°C.

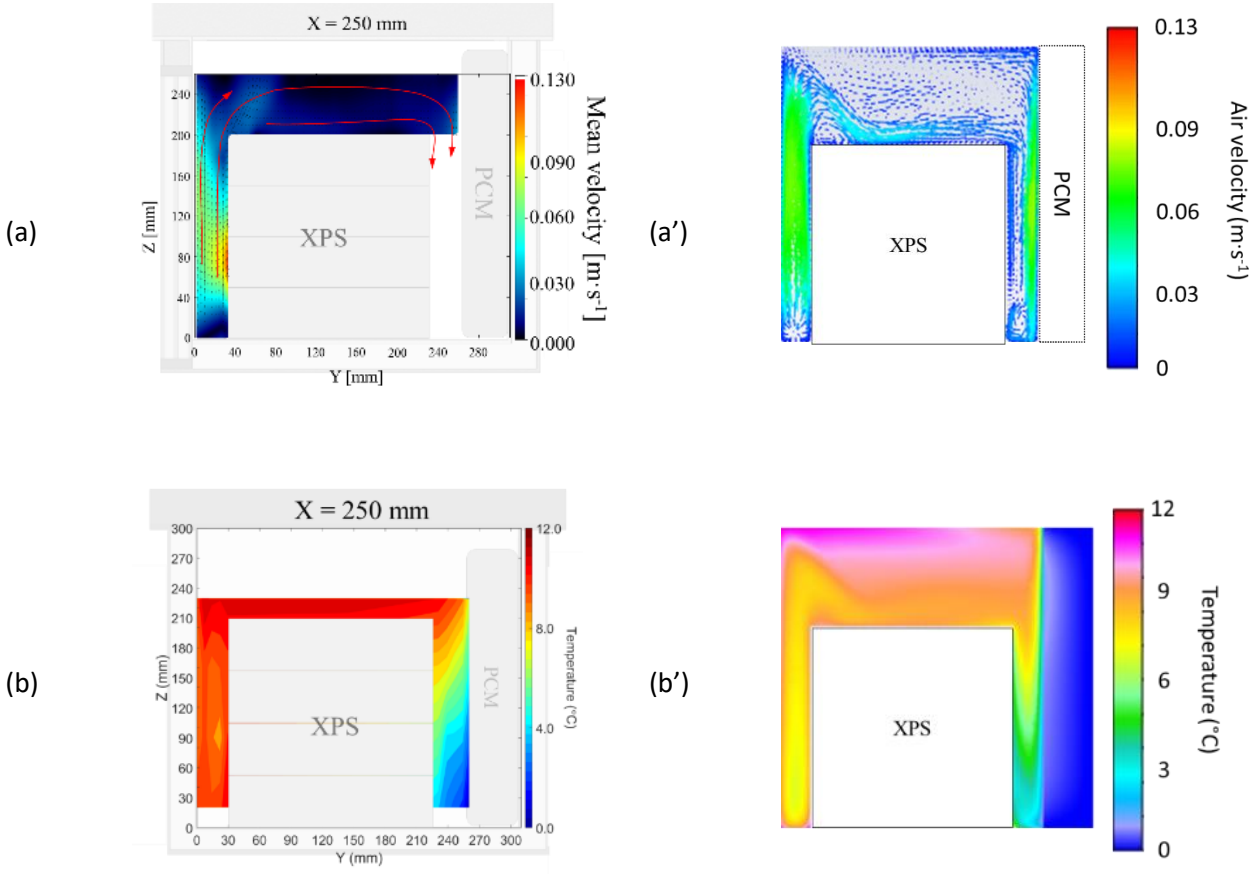

Fig. 8: (a) Experimental air velocity field and (b) experimental temperature field on the middle plane of a box loaded with XPS with PCM on a sidewall. (a') and (b') are corresponding numerical results

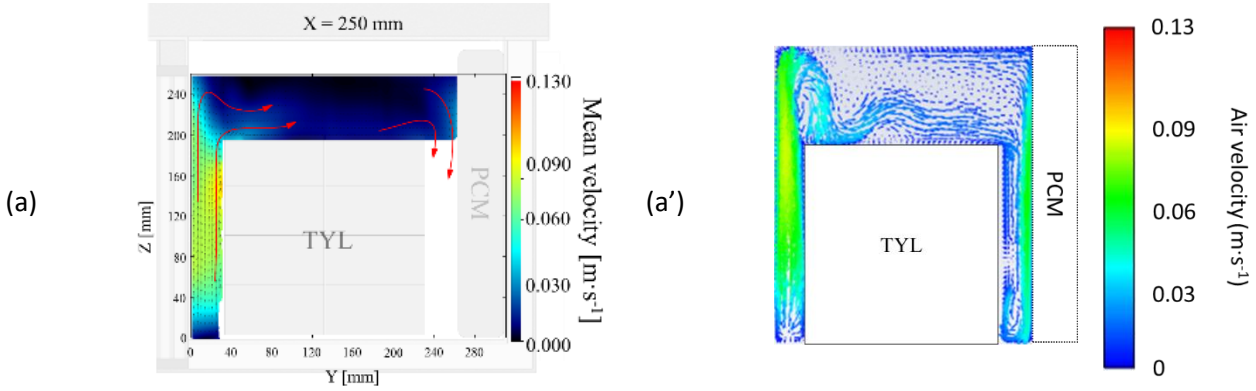

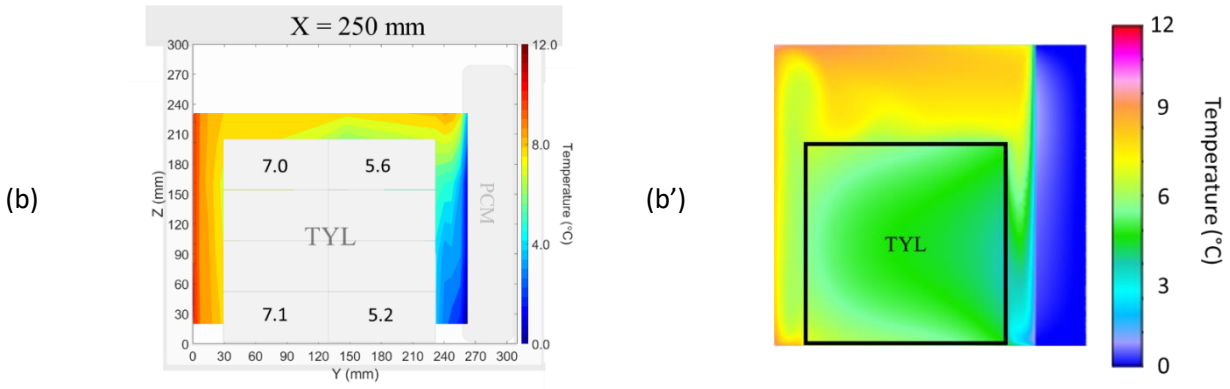

Fig. 9: (a) Experimental air velocity field and (b) experimental temperature field on the middle plane of a box loaded with Tylose with PCM on a sidewall. (a') and (b') are corresponding numerical results with initial air and Tylose temperature of 20°C and 4.4°C, respectively

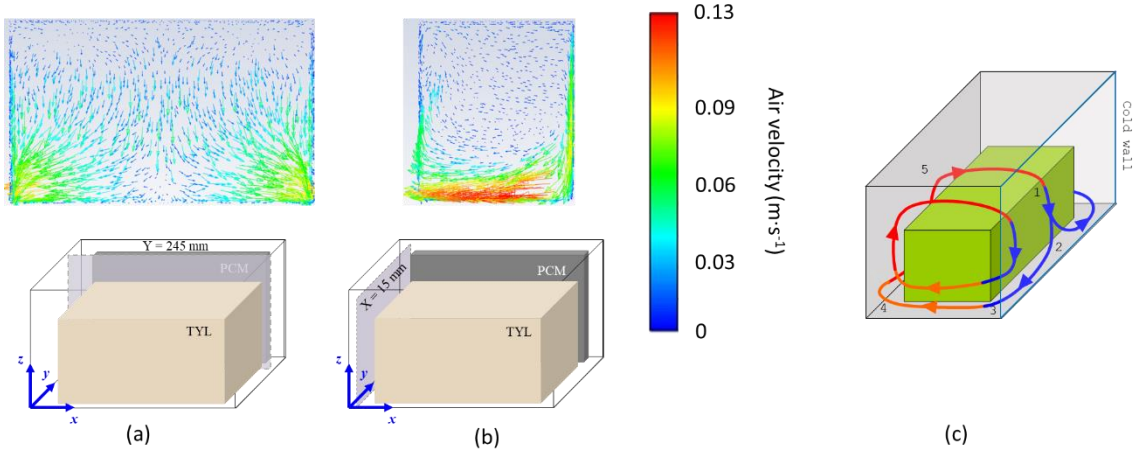

Fig. 10: Predicted air velocity field at (a) Y = 245 mm and (b) X = 15 mm, and (c) 3D airflow illustration in a loaded box with PCM on a sidewall

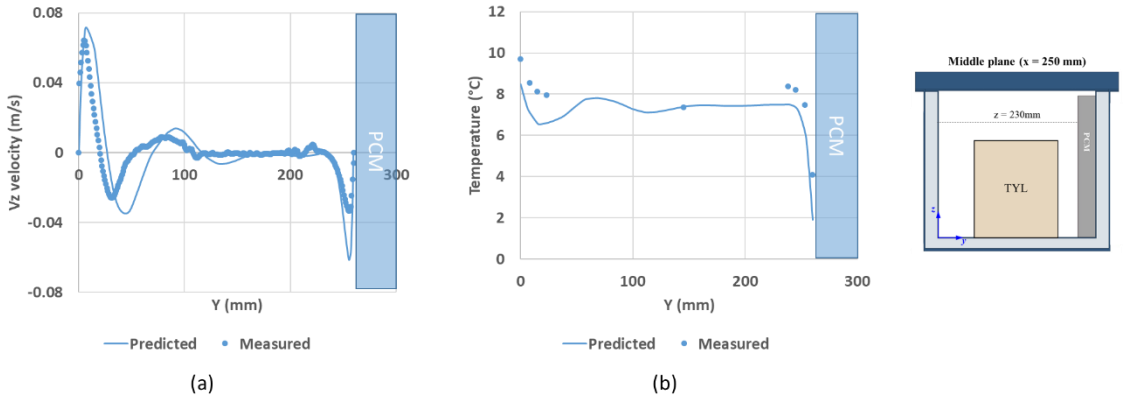

Fig. 11: Comparison between experimental and numerical results in a box loaded with Tylose with PCM on a sidewall at the middle plane and z = 230 mm of (a) air velocity in the z-direction and (b) air temperature

Fig. 12 compares the predicted and measured temperature evolution at two positions inside the Tylose slab from the beginning to 4 hours. Temperature slightly decreased at position A (at the bottom near PCM – almost the coldest position) because of convection with colder adjacent air and radiation with colder PCM surface. The temperature continuously increased at position B (at the top near a vertical wall opposite the PCM – almost the warmest position), indicating that a steady state was not reached even after 4 hours. The experimental and numerical results are in good agreement.

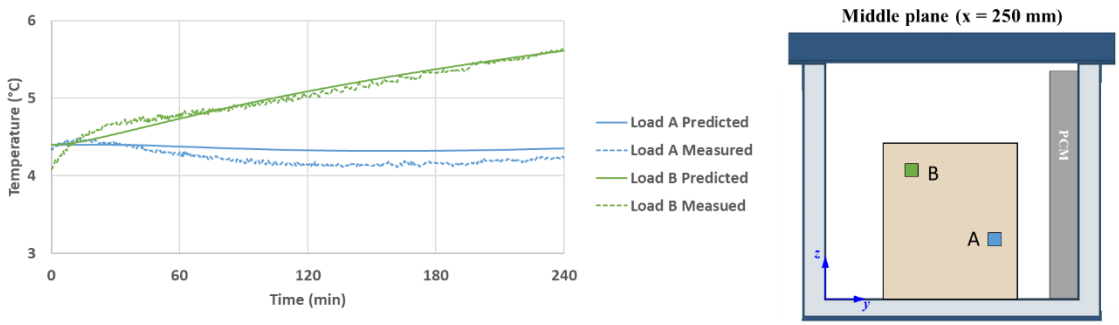

Fig. 12: Comparison between experimental and numerical results of temperature evolution at two positions in Tylose slab in a box loaded with Tylose with PCM on a sidewall from the beginning to 4 h

4.4. Air velocity and temperature profiles in a loaded box with PCM at the top

Fig. 13 and 14 show the experimental and predicted airflow patterns and temperature fields on the middle plane of the box (X = 250 mm) with PCM at the top loaded with XPS and Tylose, respectively. Cold air from the top (near the PCM) flows upward in the left gap between the side wall and load and downward in the right (PIV measurement was impossible in the right gap). The maximum measured air velocity was around 0.08 $m \cdot s^{-1}$ and 0.06 $m \cdot s^{-1}$ for the box loaded with XPS and with Tylose slab, respectively.

Since the configuration has a symmetry plane at Y = 165 mm, a symmetrical flow pattern, and temperature field could be anticipated. However, from the measurements, the air flew from left to right above the load. There seems to be a clockwise circulation loop explaining the lower measured temperature in the right gap where there was more downward flow from PCM than in the left. The numerical results shows that the airflow was asymmetrical, with a slight temperature difference between the left and right sides. The velocity was unsteady, especially near the PCM, like in the empty case with PCM at the top. In the loaded case, the downward flow chose one or another preferential pathway (through the left or right gap). This behavior is related to the non-linear term in the Navier-Stokes equations, which is responsible for a symmetry rupture (even before turbulence appears).

Simulation results gave a similar air velocity field but a slightly lower temperature than the measured field (Fig. 13a', 13b', 14a', and 14b'). Fig. 15 compares experimental data and numerical air velocity values in the z-direction and temperature at z = 230 mm in a box loaded with Tylose. As mentioned previously, comparing averaged velocity measurements with instantaneous velocity predictions is challenging.

(a)

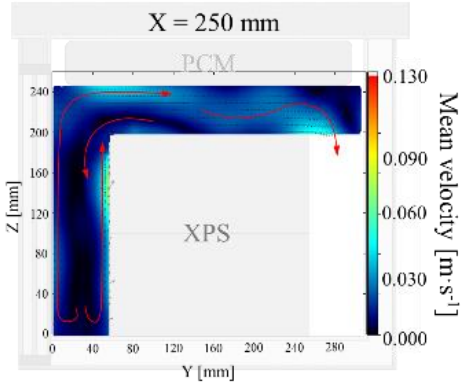

(a')

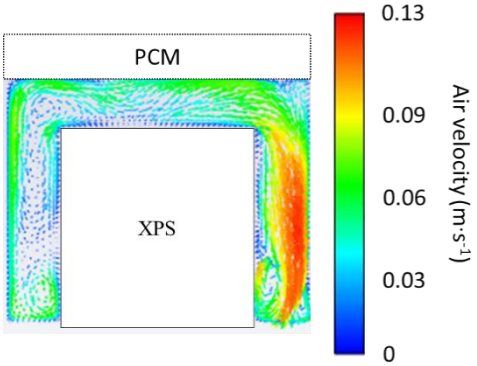

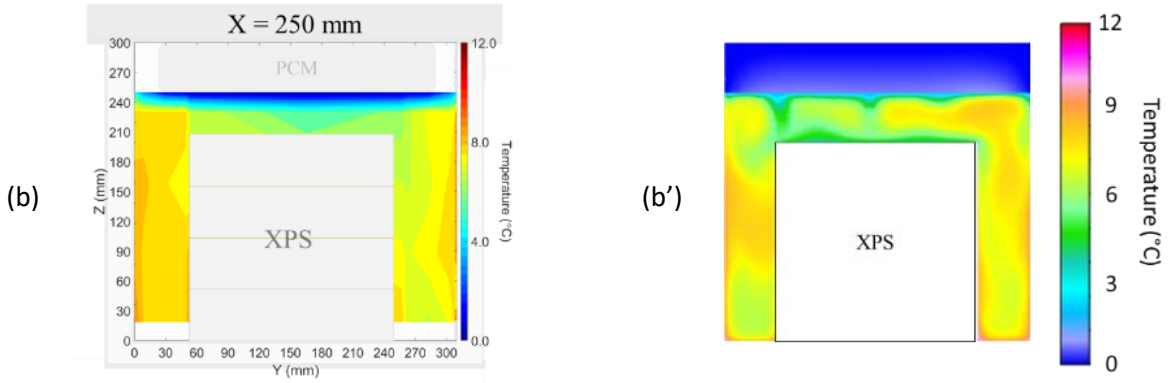

Fig. 13: (a) Experimental air velocity field and (b) experimental temperature field on the middle plane of a box with PCM at the top loaded with XPS. (a') and (b') are corresponding numerical results

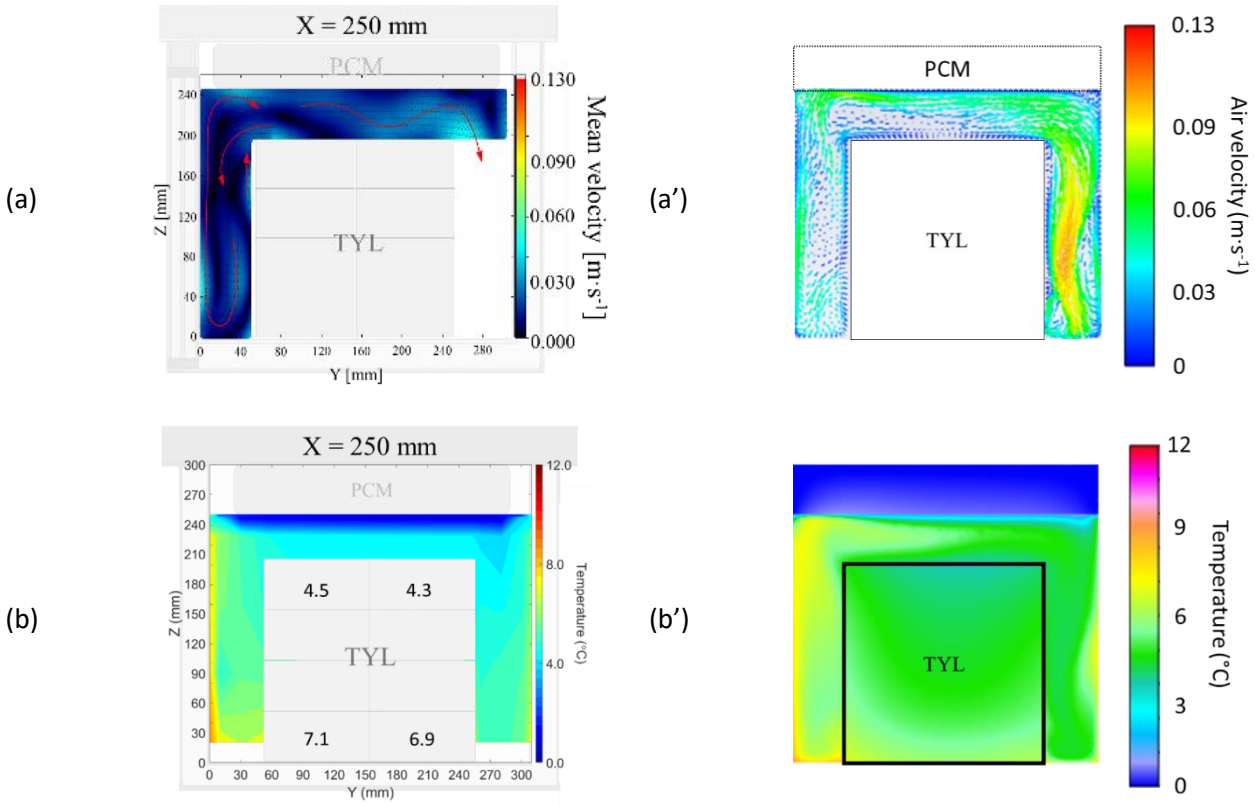

Fig. 14: (a) Experimental air velocity field and (b) experimental temperature field on the middle plane of a box with PCM at the top loaded with Tylose. (a') and (b') are corresponding numerical results with initial air and Tylose temperature of 20°C and 4.3°C, respectively.

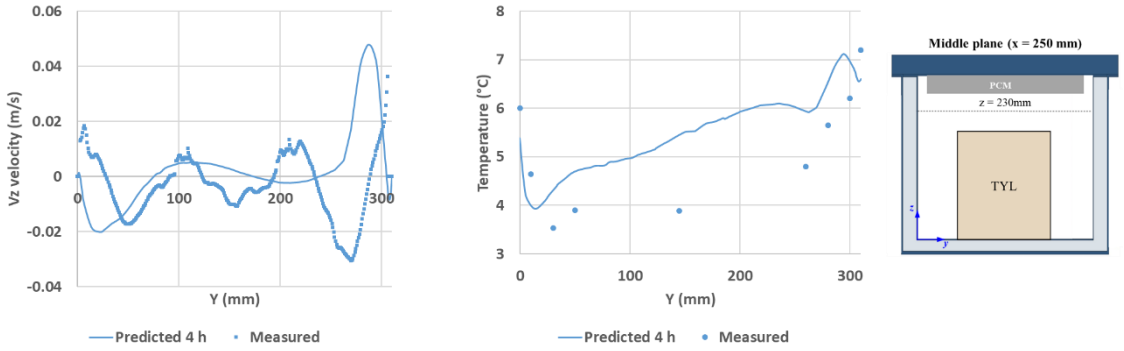

(a) (b)

Fig. 15: Comparison between experimental and numerical results in a box loaded with Tylose with PCM at the top at the middle plane and z = 230 mm of (a) air velocity in z-direction and (b) air temperature

5. CONCLUSIONS

This study implements the CFD model by ANSYS FLUENT in an insulated box equipped with PCM. The model simulates heat conduction, convection and radiation, and airflow inside the box. The model can predict the air velocity, air temperature, and product temperature evolution in the box with PCM on a sidewall with the maximum difference between predicted and measured values of 1.5°C of air temperature and 0.03 $m \cdot s^{-1}$ of air velocity. However, the model gives less accurate results in the box with PCM at the top due to flow instability and symmetry rupture, making comparisons between measurements (average values) and predictions (instantaneous fluctuating fields) challenging. Nevertheless, this model can be used to better understand variables of box configurations, e.g., box geometry, box insulation and supply chain conditions (ambient temperature).

ACKNOWLEDGEMENTS

The authors would also like to thank the Royal Thai Government Scholarship and Chulalongkorn University, Bangkok, Thailand for T. Leungtongkum's PhD scholarship. King Mongkut's Institute of Technology Ladkrabang, Thailand (contract no. KREF156402), French Embassy in Thailand, and the National Research Institute for Agriculture, Food and Environment, France are gratefully acknowledged for their financial support. This research did not receive any specific grant from funding agencies in the public, commercial, or not-for-profit sectors. Thanks to LaVision for PIV technical support.

NOMENCLATURE

c_p	Specific heat capacity ($J \cdot kg^{-1} \cdot K^{-1}$)	P	Pressure ($N \cdot m^{-2}$)
F	View factor (-)	λ	Thermal conductivity ($W \cdot m^{-1} \cdot K^{-1}$)
$\vec{g}$	Gravitational acceleration (9.81 $m \cdot s^{-2}$)	ε	Surface emissivity (-)
q_{rad}	Radiative flux ($W \cdot m^{-2}$)	σ	Stefan-Boltzmann constant = 5.67 x 10^{-8} $W \cdot m^{-2} \cdot K^{-4}$
q_{in}	Incoming radiative flux ($W \cdot m^{-2}$)	ρ	Density ($kg \cdot m^{-3}$)
T	Temperature (°C or K)	μ	Dynamic viscosity ($N \cdot s \cdot m^{-2}$)
U	Overall heat transfer coefficient ($W \cdot m^{-2} \cdot K^{-1}$)	β	Thermal expansion coefficient (K^{-1})
v	Velocity ($m \cdot s^{-1}$)		

REFERENCES

Cengel, Y.A., Ghajar, A.J., 2020. Heat and Mass Transfer: Fundamentals & Applications. McGraw-Hill Education, 1057 p.

Du, J., Nie, B., Zhang, Y., Du, Z., Wang, L., Ding, Y., 2020. Cooling performance of a thermal energy storage-based portable box for cold chain applications. J. Energy Storage, 28, 101238.

East, A., Smale, N., Kang, S., 2009. A method for quantitative risk assessment of temperature control in insulated boxes. Int. J. Refrig., 32(6), 1505–1513.

Icier, F., Ilicali, C., 2005. The use of tylose as a food analog in ohmic heating studies. J. Food Eng., 69(1), 67–77.

Laguerre, O., Flick, D., 2010. Temperature prediction in domestic refrigerators: Deterministic and stochastic approaches. Int. J. Refrig., 33(1), 41–51.

Laguerre, O., Hoang, H.M., Flick, D., 2013. Experimental investigation and modelling in the food cold chain: Thermal and quality evolution. Trends Food Sci. Technol., 29(2), 87–97.

Leungtongkum, T., Flick, D., Hoang, H.M., Steven, D., Delahaye, A., Laguerre, O., 2022. Insulated box and refrigerated equipment with PCM for food preservation: State of the art. J. Food Eng., 317, 110874.

Leungtongkum, T., Laguerre, O., Flick, D., Denis, A., Duret, S., Chaomuang, N., 2023. Experimental investigation of airflow and heat transfer by natural convection in an insulated box with a Phase Change Material using a Particle Image Velocimetry technique. J. Food Eng., 336, 111207.

Rincón-Casado, A., Sánchez de la Flor, F.J., Chacón Vera, E., Sánchez Ramos, J., 2017. New natural convection heat transfer correlations in enclosures for building performance simulation. Eng. Appl. Comput. Fluid Mech., 11(1), 340–356.
Roder, H., Perkins, R., Laesecke, A., Nieto de Castro, C., 2000. Absolute Steady-State Thermal Conductivity Measurements by Use of a Transient Hot-Wire System. J. Res. Natl. Inst. Stand. Technol., 105, 221.
Shinoda, J., Kazanci, O.B., Tanabe, S., Olesen, B.W., 2019. A review of the surface heat transfer coefficients of radiant heating and cooling systems. Build. Environ., 159, 106156.
Söylemez, E., Alpman, E., Onat, A., Hartomacıoğlu, S., 2021. CFD analysis for predicting cooling time of a domestic refrigerator with thermoelectric cooling system. Int. J. Refrig., 123, 138–149.
Vavilov, V., Burleigh, D., 2020. Infrared Thermography and Thermal Nondestructive Testing. Springer Nature, 610 p.